Initial-boundary-value problem of the self-gravitating scalar field in the Bondi-Sachs gauge

Simonetta Frittelli*
Department of Physics, Duquesne University, Pittsburgh, Pennsylvania 15282, USA

Roberto Gómez†
Pittsburgh Supercomputing Center, 300 S. Craig Ave, Pittsburgh, Pennsylvania 15213, USA
(Received 10 August 2006; revised manuscript received 30 November 2006; published 22 February 2007)

It is shown that, in the Bondi-Sachs gauge that fixes the speed of incoming light rays to the value 1, the Einstein equations coupled to a scalar field in spherical symmetry are cast into a symmetric-hyperbolic system of equations for the scalar field, lapse and shift as fundamental variables. In this system of equations, the lapse and shift are incoming characteristic fields, and the scalar field has three components: incoming, outgoing and static. A constraint-preserving boundary condition is prescribed by imposing the projection of the Einstein equation normal to the boundary at the outer value of the radial coordinate. The boundary condition specifies one of the two incoming metric fields. The remaining incoming metric field and the incoming scalar field component need to be specified arbitrarily. Numerical simulations of the scattering of the scalar field by a black hole in the nonlinear regime are presented that illustrate interesting facts about black-hole physics and the behavior of the characteristic variables of the problem.

DOI: 10.1103/PhysRevD.75.044021 PACS numbers: 04.20.Ex, 04.30.−w, 04.25.Dm

I. INTRODUCTION

The importance of the choice of gauge to the initial value problem of the Einstein equations has always been recognized, but has only recently been receiving increasing attention in view of the significant progress achieved in the last few years in numerical simulations of binary-black-hole collisions.

We report here on the properties of a newly introduced gauge for the spherically symmetric ADM problem [1]. The gauge is motivated by the Bondi-Sachs formalism [2], which is a characteristic representation (as opposed to a Cauchy representation) of the Einstein equations that has been used for accurate and stable numerical simulations of black-hole spacetimes [3,4]. In essence, the gauge is defined by the ability to control one set of characteristics of the Einstein equations, and has a considerable built-in freedom in the speed of the characteristics. For the purposes of the present work, among all possible members of the family of Bondi-Sachs gauges [1], we pick the one that makes the incoming speed of light take the value 1, for the reason that this makes the resulting ADM equations take probably their simplest form.

Additionally, in this work we allow for the presence of matter sources—again in their simplest form, namely, that of a scalar field—with the aim of demonstrating the numerical properties of the gauge in the case of a dynamical black-hole spacetime. The resulting coupled initial-value problem is shown to be well posed (which is not entirely surprising given the restriction of spherical symmetry) and the boundary value problem leads to a constraint-preserving boundary condition. We complement the analysis by presenting illustrative and enlightening results of a straightforward numerical implementation of the initial-boundary-value problem for the particular situation of the scattering of a scalar field by a black hole.

As opposed to other first-order hyperbolic renditions of the Einstein equations in spherical symmetry (see, for instance, [5]), our presentation is entirely framed within the ADM formalism and is, thus, in principle, amenable to a generalization to the general three-dimensional case with no symmetry assumptions.

II. THE BONDI-SACHS GAUGE

Given the line element in terms of the standard 3 + 1 notation [6]:

$$ds^2 = -\alpha^2 dt^2 + \gamma_{rr}(dr + \beta^r dt)^2 + r^2\gamma_T(d\theta^2 + \sin^2\theta d\phi^2), \quad (1)$$

the (advanced) Bondi-Sachs gauge [1] with unit light speed is achieved by the specification:

$$\gamma_T = 1, \quad (2)$$

$$\gamma_{rr} = \frac{\alpha^2}{(1-\beta^r)^2}. \quad (3)$$

This choice of gauge casts the line element into the form

$$ds^2 = -\frac{\alpha^2(1-2\beta^r)}{(1-\beta^r)^2}(dt+dr)^2 + \frac{2\alpha^2}{1-\beta^r}(dt+dr)dr + r^2(d\theta^2 + \sin^2\theta d\phi^2). \quad (4)$$

Clearly, a new coordinate defined as

$$v = t + r \quad (5)$$

*Electronic address: simo@mayu.physics.duq.edu
†Electronic address: gomez@psc.edu

is such that its level surfaces are null (since there is no term proportional to dr^2). Thus, the incoming light speed has the value 1. Formally changing coordinates $(t, r) \to (\upsilon, \hat{r})$ with $\hat{r} = r$ and adopting what is standard notation for line elements using a null coordinate we have

$$ds^2 = -\frac{V}{\hat{r}} e^{2\beta} d\upsilon^2 + 2e^{2\beta} d\upsilon d\hat{r} + \hat{r}^2(d\theta^2 + \sin^2\theta d\phi^2). \tag{6}$$

Here

$$e^{2\beta} \equiv \frac{\alpha^2}{1 - \beta^r} \tag{7}$$

defines β, one of the standard (original) variables of the Bondi-Sachs approach to gravitational radiation [2], which should not be confused with the shift β^r (also standard notation in the ADM approach [6] to the initial value problem in general relativity!). This assumes that $1 - \beta^r > 0$. Additionally, we have

$$\frac{V}{r} \equiv \frac{1 - 2\beta^r}{1 - \beta^r} \tag{8}$$

which defines the other relevant Bondi-Sachs variable. The (advanced) Bondi-Sachs (unit) gauge is thus defined by the requirement that the incoming light rays have speed equal to 1. (The general Bondi-Sachs gauge in advanced (retarded) form prescribes the incoming (outgoing) light speed in an arbitrary manner as a function of r [1].) The gauge is specified irrespective of coordinates, so we will make use of either the time slicing (t, r) or the null slicing $(\upsilon, \hat{r})$ depending on convenience. Our final results will be expressed in the time slicing.

III. THE EINSTEIN EQUATIONS IN THE BONDI-SACHS GAUGE

We will be interested ultimately in the coupled problem of a scalar field ϕ and the gravitational field in terms of the metric g_{ab}. This will require that we write the Einstein equations with sources for the metric, and the standard wave equation on curved spacetime for the scalar field. In this Section we derive the explicit form of the Einstein equations in the Bondi-Sachs gauge in the presence of the stress-energy tensor T_{ab} of a scalar field.

The stress-energy tensor is given by

$$T_{ab} = \nabla_a \phi \nabla_b \phi - \frac{1}{2} g_{ab} \nabla^c \phi \nabla_c \phi. \tag{9}$$

As has been shown previously [1], the Einstein equations in the Bondi-Sachs gauge in a time slicing (that is, in 3 + 1 form) are much more easily written by starting with the equations in the null slicing (the Bondi-Sachs equations) and transforming to the time slicing afterward. Thus we start with the metric element (6). As there is a one-to-one correspondence between the ADM variables (α, β^r) and the Bondi-Sachs variables (β, V), the translation from the Bondi-Sachs equations to the 3 + 1 equations is almost immediate. We follow the procedure in [1] with the only addition of a matter source.

We start with the Bondi-Sachs equations. These are

$$G_{\hat{r}\hat{r}} = 8\pi T_{\hat{r}\hat{r}} \tag{10}$$

for β, and

$$g^{\hat{r}\hat{r}} G_{\hat{r}\hat{r}} + 2g^{\upsilon\hat{r}} G_{\upsilon\hat{r}} = 8\pi(g^{\hat{r}\hat{r}} T_{\hat{r}\hat{r}} + 2g^{\upsilon\hat{r}} T_{\upsilon\hat{r}}) \tag{11}$$

for V. Explicitly they read, respectively,

$$\beta_{,\hat{r}} = 2\pi\hat{r}\phi_{,\hat{r}}\phi_{,\hat{r}} \tag{12a}$$

$$V_{,\hat{r}} = e^{2\beta}. \tag{12b}$$

These are evolution equations for β and V along null geodesics on the slice of fixed value of υ. Data for these equations consists of the values of β and V at a surface of fixed value of $\hat{r}$. The data are not free, however, as there is one constraint arising from the component

$$G^{\hat{r}}_{\upsilon} = 8\pi T^{\hat{r}}_{\upsilon} \tag{13}$$

of the Einstein equations, which is preserved by the evolution Eqs. (12). This has the explicit form:

$$2V\beta_{,\upsilon} - V_{,\upsilon} = 8\pi\hat{r}^2\left(\phi_{,\upsilon}\phi_{,\upsilon} + \frac{V}{\hat{r}}\phi_{,\upsilon}\phi_{,\hat{r}}\right). \tag{14}$$

The constraint thus takes the form of an evolution equation restricted to the starting data surface. In practice, one may prescribe freely the value of V, for instance, all along the surface of fixed value of $\hat{r}$, and then use this constraint to calculate the values of β on this surface, of which only the value at $\upsilon = 0$ is needed.

In order to obtain an initial value problem in a time slicing, we now transform the coordinates from $(\upsilon, \hat{r})$ into (t, r) and the variables from (β, V) to (α, β^r) by means of (7) and (8). The result is

$$\dot{\alpha} - \alpha_{,r} = -\alpha\left(\frac{\alpha^2 - 1 + 2\beta^r}{2r} + 2\pi r(\dot{\phi} - \phi_{,r})^2\right) \tag{15a}$$

$$\dot{\beta}^r - \beta^r{}_{,r} = \frac{1 - \beta^r}{r}(\alpha^2 - 1 + 2\beta^r). \tag{15b}$$

These are first-order time-dependent evolution equations for the lapse and shift requiring data at $t = 0$. The principal terms of the equations are decoupled for the lapse and shift. This means that the problem is well posed and that the lapse and shift themselves are characteristic fields [7]. From the equations themselves one can read the value of the characteristic speeds. Both the lapse and shift propagate inwardly at speed of value 1 (the incoming light speed). The problem is, trivially, symmetric hyperbolic [7].

The data at $t = 0$ are not free, but they must satisfy a constraint that arises from translating Eq. (14) into the ADM language and coordinates. This is

$$0 = \mathcal{C} \equiv \beta^r{}_{,r} + \frac{1-2\beta^r}{\alpha}\alpha_{,r} + \frac{(\alpha^2 - 1 + 2\beta^r)}{2r} - 2\pi r(\dot{\phi}^2 + (1-2\beta^r)\phi_{,r}{}^2). \quad (16)$$

This is a first-order differential constraint on the lapse and shift. As a consequence of the Bianchi identities and the conservation of the stress-energy tensor one has $\nabla_a(G^{ab} - 8\pi T^{ab}) = 0$ which implies a propagation equation of the form

$$\dot{\mathcal{C}} - \mathcal{C}_{,r} = \ldots \quad (17)$$

for the constraint, where ... represent undifferentiated terms in the constraint itself, and terms proportional to the evolution equations (15) or their derivatives. As a result, the constraint propagates inwardly at the speed of light whenever the evolution equations (15) are satisfied. Thus, the constraint need only be imposed on the initial values of the lapse and shift.

IV. THE WAVE EQUATION IN THE BONDI-SACHS GAUGE

In this Section we derive the explicit form of the wave equation in curved spacetime in the Bondi-Sachs gauge. As the wave equation is a scalar equation, it is convenient to use the null slicing $(v, \hat{r})$ at first, as the metric and connection coefficients are much simpler in null coordinates, and eventually transform to the time slicing.

The wave equation has the form

$$g^{ab}\nabla_a\nabla_b\phi = 0. \quad (18)$$

Explicitly, using the line element (6), this reads

$$2\phi_{,v\hat{r}} + \frac{V}{\hat{r}}\phi_{,\hat{r}\hat{r}} + \left(\frac{V_{,\hat{r}}}{\hat{r}} + \frac{V}{\hat{r}^2}\right)\phi_{,\hat{r}} + \frac{2}{\hat{r}}\phi_{,v} = 0. \quad (19)$$

By virtue of the Einstein equations in the null slicing, Eqs. (12), the quantity $V_{,\hat{r}}$ can be substituted in terms of undifferentiated terms:

$$2\phi_{,v\hat{r}} + \frac{V}{\hat{r}}\phi_{,\hat{r}\hat{r}} + \left(\frac{e^{2\beta}}{\hat{r}} + \frac{V}{\hat{r}^2}\right)\phi_{,\hat{r}} + \frac{2}{\hat{r}}\phi_{,v} = 0. \quad (20)$$

Now we transform coordinates from $(v, \hat{r})$ into (t, r):

$$-\left(2 - \frac{V}{r}\right)\ddot{\phi} + 2\left(1 - \frac{V}{r}\right)\dot{\phi}_{,r} + \frac{V}{r}\phi_{,rr} + \frac{2}{r}\dot{\phi} + \left(\frac{e^{2\beta}}{r} + \frac{V}{r^2}\right)(\phi_{,r} - \dot{\phi}) = 0. \quad (21)$$

Finally, we express the Bondi-Sachs variables (β, V) in terms of the ADM variables (α, β^r) via Eqs. (7) and (8), obtaining:

$$0 = \ddot{\phi} - 2\beta^r\dot{\phi}_{,r} - (1-2\beta^r)\phi_{,rr} - \frac{2}{r}(1-\beta^r)\dot{\phi} - \frac{\alpha^2 + 1 - 2\beta^r}{r}(\phi_{,r} - \dot{\phi}). \quad (22)$$

V. THE WAVE EQUATION COUPLED TO THE EINSTEIN EQUATIONS IN THE BONDI-SACHS GAUGE

As the combined problem stands, Eqs. (15) and (22), it makes sense as a hyperbolic Cauchy problem for the metric variables and the scalar field ϕ. We can reduce the differential order of the problem without affecting its principal part, simply by defining the derivatives of the field ϕ as new variables:

$$P \equiv \dot{\phi}, \quad (23a)$$

$$Q \equiv \phi_{,r}. \quad (23b)$$

Substituting everywhere into (15) and (22), we find

$$\dot{\alpha} = \alpha_{,r} - \alpha\left(\frac{\alpha^2 - 1 + 2\beta^r}{2r} + 2\pi r(P-Q)^2\right) \quad (24a)$$

$$\dot{\beta}^r = \beta^r{}_{,r} + \frac{1-\beta^r}{r}(\alpha^2 - 1 + 2\beta^r) \quad (24b)$$

$$\dot{P} = 2\beta^r P_{,r} + (1-2\beta^r)Q_{,r} + \frac{\alpha^2 + 1 - 2\beta^r}{r}(Q-P) + \frac{2}{r}(1-\beta^r)P \quad (24c)$$

$$\dot{Q} = P_{,r} \quad (24d)$$

$$\dot{\phi} = P. \quad (24e)$$

The coupled system of equations has a block-diagonal principal part:

$$\dot{\alpha} = \alpha_{,r} \quad (25a)$$

$$\dot{\beta}^r = \beta^r{}_{,r} \quad (25b)$$

$$\dot{P} = 2\beta^r P_{,r} + (1-2\beta^r)Q_{,r} \quad (25c)$$

$$\dot{Q} = P_{,r} \quad (25d)$$

$$\dot{\phi} = 0 \quad (25e)$$

which implies that the characteristic speeds and fields of the metric equations are decoupled from those of the scalar field problem. Thus, the eigenvalue problem of each block can be solved separately. We already know that the first two equations in this set have incoming characteristic speed of 1 with α and β^r as the characteristic fields. The last three equations, corresponding to the scalar field problem, have the following characteristic speeds and eigenvectors, expressed in the form $(\phi, P, Q)^t$:

(i) Speed of 0, with eigenvector $(1, 0, 0)^t$ and corresponding characteristic field

$$\hat{U}^0 \equiv \phi. \quad (26)$$

(ii) Incoming speed of 1 (light speed), with eigenvector $(0, 1, 1)^t$ and corresponding incoming characteristic field

$$\hat{U}^- \equiv P + (1 - 2\beta^r)Q. \tag{27}$$

(iii) Speed of $1 - 2\beta^r$ (light speed), with eigenvector $(0, -1 + 2\beta^r, 1)^t$ and corresponding characteristic field

$$\hat{U}^+ \equiv P - Q. \tag{28}$$

This field will be outgoing for values of r such that $1 - 2\beta^r > 0$, static wherever $1 - 2\beta^r = 0$, and incoming for values of r such that $1 - 2\beta^r < 0$.

There are two constraints to be imposed on the initial data:

$$0 = \beta^r{}_{,r} + \frac{1 - 2\beta^r}{\alpha}\alpha_{,r} + \frac{(\alpha^2 - 1 + 2\beta^r)}{2r} - 2\pi r(P^2 + (1 - 2\beta^r)Q^2) \tag{29}$$

$$0 = \phi_{,r} - Q. \tag{30}$$

The coupled problem is, thus, strongly hyperbolic and, therefore, well posed. This may seem unexpected, as spherically symmetric renditions of the ADM equations have been widely used by now, especially for numerical applications. Most applications have used versions of the reduced problem in which the ADM sector of the equations are ordinary radial equations (as in [8], for instance). In cases when time-dependent versions of the equations have been used, their well-posed character has not been recognized. In particular, the work of [9] has a very close relationship with the present work. In [9], the authors examine the ADM problem related to the ingoing Bondi-Sachs problem within the context of Cauchy-characteristic matching, in which a 3 + 1 scheme is used to integrate the Einstein equations in a finite region, and characteristic approaches are used outside the outer radius and within the inner radius. As opposed to our present work, in the ''Cauchy region'' the authors use γ_{rr} and a component of the extrinsic curvature K^θ_θ as fundamental variables for the ADM equations. As the transformation from these fields to lapse and shift is one-to-one, the ADM equations for these variables (numbered (4.4) and (4.5) in [9]) are equivalent to (24a) and (24b). In contrast with our choice, the resulting characteristic speeds are not constant and the equations have a significantly more complicated appearance.

VI. BOUNDARY CONDITIONS

One of the main applications of the coupled system of Eqs. (24) would be for numerical simulations of black-hole spacetimes. Such simulations usually implement a numerical code in a finite spatial region, extending from an inner radius $r_{\rm in}$ out to an outer radius $r_{\rm out}$, and require appropriate handling of boundary values. As the system is well posed and all the characteristic fields are known, appropriate boundary conditions can be found in this case.

A. Outer boundary

All the incoming fields (traveling towards decreasing values of r) require the prescription of values at the outer radius $r_{\rm out}$ [7]. In this case, this includes the variables α, β^r and U^-. The boundary values of the incoming variables at the outer radius are not completely arbitrary, however, due to the presence of the constraint $\mathcal{C}$ which itself propagates inwardly. The presence of an incoming constraint implies the existence of *one constraint-preserving boundary condition at the outer radius* [10]. In this case, the constraint-preserving boundary condition is readily spotted, as it must be the same as the constraint (14) of the Bondi-Sachs form of the Einstein equations. Changing coordinates from $(v, \hat{r})$ into (t, r) and transforming the Bondi-Sachs metric variables into ADM metric variables via (7) and (8) we have

$$\dot{\beta}^r + \frac{(1 - 2\beta^r)}{\alpha}\dot{\alpha} = 4\pi r P(\beta^r P + (1 - 2\beta^r)Q) \tag{31}$$

This boundary condition is exactly the component $G^{\hat{r}}_v = 8\pi T^{\hat{r}}_v$ of the Einstein equations in coordinates $(v, \hat{r})$, which is equal to the component $G^r_t = 8\pi T^r_t$ in coordinates (t, r). So one can see that the constraint-preserving boundary condition is the projection of the Einstein equation perpendicularly to the boundary of fixed value of r, as could be expected [11]. Equivalently [11], this boundary condition can also be found by substituting, in $\mathcal{C}$, all the radial derivatives in terms of time derivatives by means of the evolution equations (24). This procedure for finding the boundary condition provides a basis for interpreting the boundary condition as the vanishing of the constraint on the boundary.

The boundary condition prescribes the time derivative of one (or a combination) of the two metric incoming fields, and is interpreted as an evolution equation along the outer boundary for either one of the two incoming metric fields. The remaining metric field, as well as the incoming scalar field $\hat{U}^-$, are arbitrary, but their values must be prescribed in order for there to exist a unique solution. The outgoing field $\hat{U}^+$ and the static field ϕ cannot be prescribed arbitrarily, as their boundary values at the outer radius are determined by their own values on the initial slice [7].

As per inspection of Eq. (31), an outer boundary condition linking the values of the lapse and shift remains even in the vacuum case, namely, when $\phi \equiv 0$ throughout in the region of interest. Of course, as per well-known theorems, there is no gravitational radiation in the spherically symmetric vacuum case, and the only solution of the Einstein equations is the Schwarzschild metric, up to coordinate transformations. So the question arises as to what role the

boundary condition plays in the vacuum case. The answer lies in the fact that in this (as in any) initial-boundary value problem, the solution is not entirely determined by the initial data, but depends on incoming boundary values as well. Any prescription of initial data consistent with the constraint (16) in vacuum corresponds to a slice of Schwarzschild spacetime in a particular choice of radial and time coordinates. However, the choice of coordinates is not completely specified by the data on one slice (a freedom of one function of a real variable remains). If in addition one were to prescribe boundary values for the lapse and shift that were not consistent with the boundary condition (31), there would be no global coordinate transformation of the radial and time coordinates (with the appropriate smoothness) that would take the resulting solution into the standard form of the Schwarzschild metric. The boundary condition (31) plays as leading a role as the initial constraint in guaranteeing that there exists a coordinate transformation that takes the solution of the initial-boundary value problem into the standard form of the Schwarzschild metric.

B. Inner boundary

At the inner boundary, values must be prescribed for all outgoing fields (traveling towards increasing values of r) in order to completely specify the solution [7]. There is only one outgoing field in this problem and it is a scalar field component, $\hat{U}^+$. The boundary values of the scalar field components are not determined by the Einstein equations; in fact, Eq. (31) must be an identity when applied at the inner boundary $r_{\rm in}$. Thus the value of $\hat{U}^+ = P - Q$ can be specified arbitrarily, in generic situations where its characteristic speed remains "outgoing", i.e., so long as $1 - 2\beta^r > 0$ for all values of r in the interval $[r_{\rm in}, r_{\rm out}]$.

This does not apply to black-hole situations, where light rays are all incoming in the black-hole region. A black-hole situation results in our scheme when the outgoing characteristic speed $1 - 2\beta^r$ changes sign in the interval $r_{\rm in} < r < r_{\rm out}$, as it would if the underlying spacetime was, for instance, Schwarzschild. In a black-hole situation, the characteristic speed of the field $\hat{U}^+ = P - Q$ turns from outgoing, to zero, to incoming as the value of r decreases within an interval containing the radius of the apparent horizon [12], as illustrated in Fig. 1. Thus, if the inner radius $r_{\rm in}$ is smaller than the radius of the apparent horizon, the inner boundary values of all the fields in the problem are determined by their initial data and cannot be assigned arbitrarily. In practice, this means that the boundary values must be calculated in a manner consistent with the initial data, otherwise the solution-generating mechanism will be unstable. One way to obtain consistent inner boundary values is explained in Sec. VII.

Because no characteristic fields propagate towards increasing values of r at the inner boundary in a black-hole situation, the advanced Bondi-Sachs gauge belongs to the type of horizon-penetrating gauges of widespread use in numerical simulations [13].

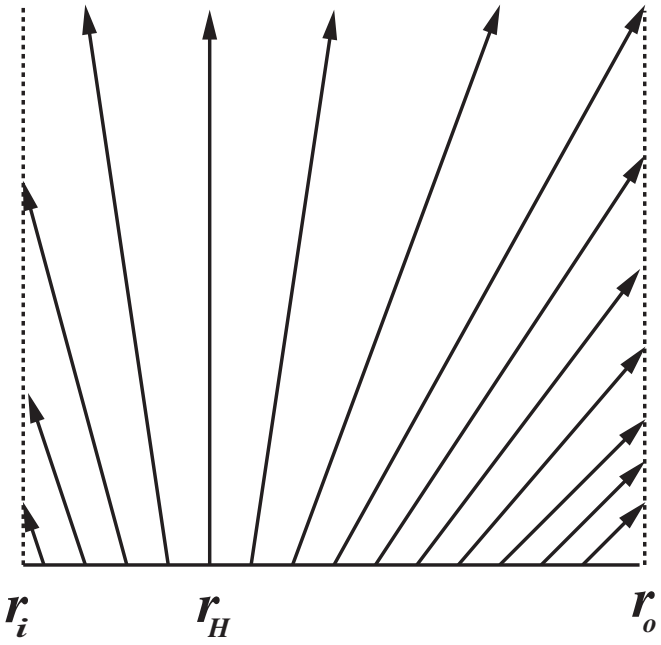

FIG. 1. Propagation of the characteristic field U^+ in a black-hole situation. The apparent horizon is at $r = r_H$. The characteristic speed $1 - 2\beta^r$ is positive for $r > r_H$, zero at $r = r_H$ and negative for $r < r_H$. The field travels towards increasing values of r outside of the horizon, and towards decreasing values of r within the horizon.

VII. NUMERICAL APPLICATION

To illustrate the suitability of the problem to numerical simulations, we apply the system of equations derived in Sec. V to the problem of the scattering of a scalar field by a black hole, starting with Eqs. (24) but written in terms of $g = r\phi$ and the associated characteristic fields $U^+ = g_{,t} - g_{,r}$, $U^- = g_{,t} + (1 - 2\beta^r)g_{,r}$. In terms of these variables the equations read

$$\dot{\alpha}^2 = \alpha^2_{,r} - \alpha^2\left[\frac{\alpha^2 - 1 + 2\beta^r}{r} + \frac{4\pi}{r}\left(U^+ + \frac{g}{r}\right)^2\right] \quad (32a)$$

$$\dot{\beta}^r = \beta^r_{,r} + \frac{1 - \beta^r}{r}(\alpha^2 - 1 + 2\beta^r) \quad (32b)$$

$$\dot{U}^+ = -(1 - 2\beta^r)U^+_{,r} \quad (32c)$$

$$- \frac{\alpha^2 - 1 + 2\beta^r}{r}\left(U^+ + \frac{g}{r}\right) \quad (32d)$$

$$\dot{U}^- = U^-_{,r} - \frac{\alpha^2 - 1 + 2\beta^r}{r}\left(U^- + \frac{g}{r}\right) \quad (32e)$$

$$\dot{g} = \frac{U^- + (1 - 2\beta^r)\hat{U}^+}{2(1 - \beta^r)} \quad (32f)$$

with two initial constraints

$$0 = (1-2\beta^r)\alpha_{,r}^2 + 2\alpha^2\beta_{,r}^r + \frac{\alpha^2}{r}(\alpha^2 - 1 + 2\beta^r) - \frac{4\pi\alpha^2}{r}\left[(\dot{g})^2 + (1-2\beta^r)\left(g_{,r} - \frac{g}{r}\right)^2\right] \quad (33a)$$

$$g_{,r} = \frac{U^- - U^+}{2(1-\beta^r)}, \quad (33b)$$

and one constraint-preserving outer boundary condition

$$0 = (1-2\beta^r)\dot{\alpha}^2 + 2\alpha^2\dot{\beta}^r - \frac{8\pi}{r}\alpha^2\dot{g}\left[\beta^r\dot{g} + (1-2\beta^r)\left(g_{,r} - \frac{g}{r}\right)\right]. \quad (34)$$

In the right-hand side of Eqs. (33a) and (34), the occurrences of $\dot{g}$ and $g_{,r}$ are to be read only as a short-hand for the right-hand sides of Eqs. (32f) and (33b), respectively. In Eqs. (32) and for the remainder of this work, we use the notation $\dot{\alpha}^2 = \partial(\alpha^2)/\partial t$.

A. Initial data

We construct initial data that satisfy the constraints by setting β^r to the form corresponding to a Schwarzschild black hole of mass M,

$$\beta^r = \frac{2M}{r+2M}. \quad (35)$$

For all the simulations that follow, the value of M is set to 1. The ansatz for the initial profile for g_0 is a compact pulse of the form

$$g_0 = A\frac{[(r-r_1)(r-r_2)]^4}{[\frac{1}{2}(r_2-r_1)]^8}, \quad (36)$$

at $t = 0$, for $r_{\rm in} < r_1 < r < r_2 < r_{\rm out}$, and $g = 0$ elsewhere. We pick values for U^+ and U^- that make $\dot{g} = 0$ on the initial slice. In practice, we evaluate the radial derivative $g_{,r}$ numerically from the ansatz g_0, which gives us the left-hand side of Eq. (33b), and set $\dot{g} = 0$ in the left-hand side of Eq. (32f). With the given values of β^r as above, the initial values of U^+ and U^- are then determined from the two resulting linear equations.

B. Integration scheme

Our integration scheme is guided by the following perhaps nontrivial observation pertaining to a Schwarzschild simulation. In the absence of a scalar field, namely, for a Schwarzschild black hole, the lapse α and the shift β^r are related by $\alpha^2 = 1 - \beta^r$. Using $X \equiv \alpha^2$, the evolution equations for α and β^r are thus equivalent to the single PDE

$$\dot{X} = X_{,r} - \frac{X(1-X)}{r}, \quad (37)$$

and the solution is $X = r/(r+2M)$. This has the form of a compactified radial coordinate frequently used in characteristic evolution [14]. By expressing the radial derivatives as $\partial_r = X_{,r}\partial_X$, it is very straightforward to construct an algorithm that will automatically satisfy $\dot{\alpha}^2 = \dot{\beta}^r = 0$ for Schwarzschild, regardless of what discretization stencil we choose for the radial derivatives, or of what particular time-integration method we implement. The use of this compactified coordinate allows us to implement an integration scheme that, when turning off the matter sources, simulates a Schwarzschild black hole to an extreme accuracy for any length of time.

In our implementation, we use a grid based on the compactified coordinate X with $M = 1$. The radial grid points are given by $X_i = X_{\rm in} + (i-1)\Delta X$, for $i = 1 \ldots N$, where $\Delta X = (X_{\rm out} - X_{\rm in})/(N-1)$. We solve the coupled system, Eqs. (32) by writing, e.g.

$$U^+_{,r}|_i = U^+_{,X}X_{,r}|_i. \quad (38)$$

The Jacobian $X_{,r}$ at the point X_i is computed analytically, and the derivative $U^+_{,X}$ is approximated by upwind second-order finite differences. We compute the derivative of U^+, which changes its direction of propagation at the horizon, by choosing between left-sided (D_-U^+) and right-sided (D_+U^+) finite differences according to the sign of the characteristic speed $v = 1 - 2\beta^r$,

$$vU_{,X}|_i = H(v)vD_+U_i + H(-v)vD_-U_i \quad (39)$$

Only right-sided derivatives are needed for the fields α, β^r and U^-. We integrate the resulting ODEs in time with an explicit fourth-order Runge-Kutta method [15]. Since the time-integration method is explicit, the time-step is limited by the Courant condition, which, by inspection of the principal part of Eq. (32), is $\Delta t \leq \Delta r$. In our simulations we have kept the time-step constant throughout the simulation, and given by $\Delta t = \epsilon\Delta r_0$, where Δr_0 is the grid spacing at the left edge of the grid (the smallest value of Δr). We set $\epsilon = \frac{1}{4}$, within the stable range for the scheme used.

The use of the compactified radial coordinate X leads to increased resolution near the black hole. On the down side, grid points are spread further apart towards the outer edge. This could pose a potential problem if we were to extend the radial grid sufficiently far out, in sharp contrast with the characteristic formulation, where the outer boundary can be put at null infinity. In our simulations, the outer edge of the grid is at $r = 20$, not far enough to encounter any problems, i.e.: the fields are well resolved in the entire grid (refer to Subsection VII F for details).

C. Inner boundary

We set the inner boundary inside the horizon ($r_{\rm in} < 2M$) of the initial black hole, typically at $r_{\rm in} = \frac{3}{2}M$. Since at the inner boundary all fields are either ingoing or have zero characteristic speed, it is consistent to approximate the radial derivatives in Eqs. (32) with upwind (one-sided)

finite difference stencils using grid points at, and to the right of, the boundary.

D. Outer boundary

At the outer boundary, which we take to be at $r_{\rm out} = 20M$, we enforce the constraint-preserving boundary condition by solving (34) for α, given β^r, U^+ and U^-. Because the field U^+ is outgoing, it is consistent to use an upwind discretization at the boundary of the corresponding evolution equation, i.e. involving points at, and to the left of, the boundary. The values of the incoming fields β^r and U^- can be specified freely. Currently, little if anything is known about how boundary values relate to specific physically motivated solutions of the Einstein equations with given initial data. For actual simulations, thus, some reasonable assumption must be made, whose validity can only be verified after the fact. In practice we achieve a stable evolution, with no significant reflections at the outer boundary, by calculating the boundary values of the incoming variables using the evolution equations (32b) and (32e) with the radial derivatives entering in the evolution equations approximated at the last grid point with left-sided stencils (as opposed to right-sided stencils, which are used in the interior points). Physically, this corresponds loosely to the condition of an "open" boundary (like the open end of a pipe in the case of sound waves).

E. Tests of convergence

To calibrate the accuracy of the numerical implementation, given initial data, we perform simulations at increasing resolution and compare the results. The initial data in these tests are given by a pulse (36) with amplitude $A = 5 \times 10^{-2}$, and support between $r_1 = 4$ and $r_2 = 8$. We carry out simulations on 200, 400, 800 and 1600 grid points, up to a fixed time $t_f = 4.0$ (for a total of 17 400 time-steps on the finest grid). For each resolution but the finest, we estimate the error by subtracting the field values at t_f on the finest grid. The dominant source of error is the (second-order) spatial discretization of the radial derivatives, rather than the (fourth-order) time-integration scheme. Each time we refine the grid by a factor of 2, we expect the error to decrease by a factor of 4. Figure 2 shows that this is the case, as the various errors (the difference between the numerical solution at time t_f for each grid, minus the values on the same set of points on the reference run at 1600 points), when scaled up by the appropriate factor (1,4, and 16, respectively), overlap. We illustrate here the convergence of the algorithm only with the characteristic field ϕ because it is the most intuitive, but we have verified the convergence rate of all fields. Performing runs at successively finer resolutions serves not only to validate the convergence of the numerical algorithm; it also allows us to put error bars in the results. In all subsequent graphs in this article a grid of 3000 points is used.

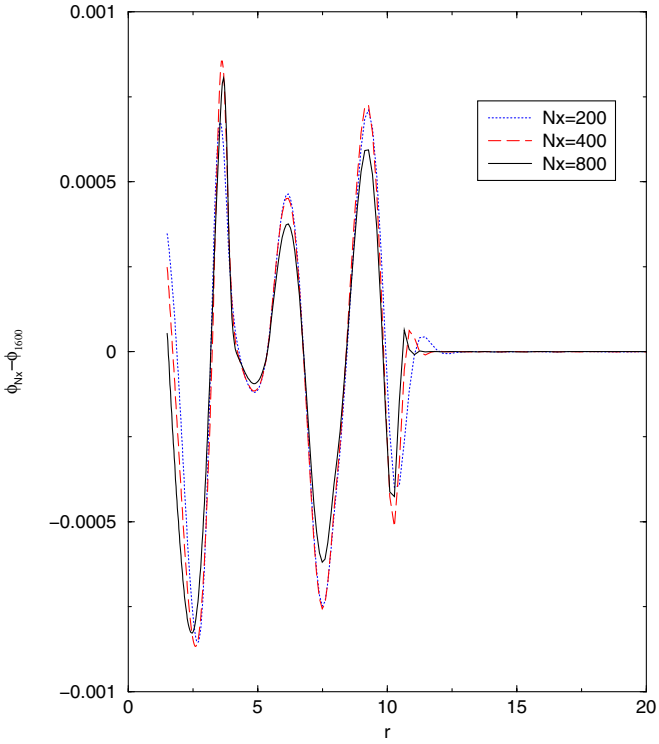

FIG. 2 (color online). Error in ϕ at $t = 4.0$, for initial data consisting of a pulse (36) with amplitude $A = 5 \times 10^{-2}$, and support between $r_1 = 4$ and $r_2 = 8$. We plot the difference between values obtained on grids with $N = 200, 400, 800$ points, and a reference simulation with $N = 1600$ points. The error values for 400 and 800 points have been scaled by a factor of 4 and 16, respectively. The agreement shows the code is second-order convergent, as dictated by the order of discretization of the radial derivatives.

F. Evolution of the characteristic fields in the nonlinear regime

Using the same initial radial profile for g as in the previous subsection, we track the evolution of the characteristic fields ϕ, U^+, U^-, α and β^r.

Figure 3 shows ϕ as a function of r and t, with the initial value at the bottom right edge of the figure (time running towards the upper left corner). One can see that the initial pulse splits into an incoming and an outgoing secondary pulses, with the incoming secondary pulse reaching the inner boundary of the grid at about $t = 7$, and the outgoing pulse leaving the numerical grid by $t = 25$. The reason why a characteristic field with zero speed like ϕ shows secondary traveling behavior is to be found in the coupling of ϕ to traveling characteristic fields through undifferentiated terms in the right-hand side of Eq. (32f). The mathematics of this phenomenon are similar to the effects of driving forces in the simple harmonic oscillator.

This traveling behavior in ϕ has an added benefit to simulations based on a compactified radial coordinate, as it helps offset the loss of resolution that would otherwise result at the outer edge of the grid. The behavior of the

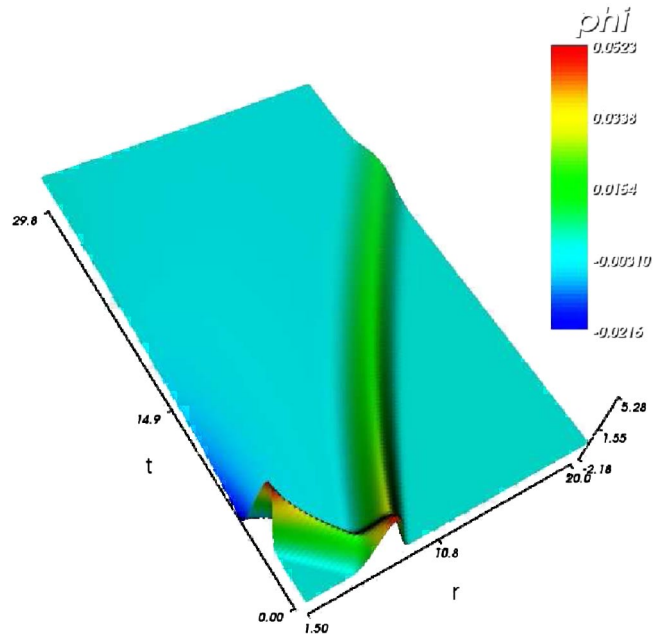

FIG. 3 (color online). Evolution of ϕ, scaled by a factor of 100, from $t = 0$ until $t = 25$, by which time the outgoing component of the pulse has crossed the outer grid boundary.

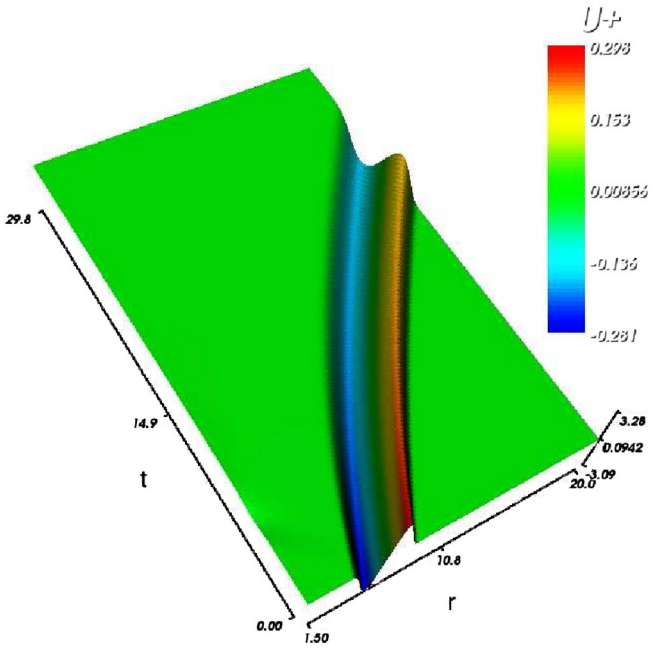

FIG. 4 (color online). Evolution of U^+, scaled by a factor of 10, from $t = 0$ until $t = 25$, by which time the pulse has crossed the outer grid boundary.

outgoing component of ϕ is driven entirely by the propagation of U^+, from the right–hand side of Eq. (32f). The characteristic speed of U^+ increases with r, from zero at the apparent horizon to roughly 0.8 at the outer edge. This coordinate dependence of the propagation speed causes the outgoing pulse to expand. By the time the outer edge of the outgoing pulse reaches $r = 20M$, at approximately $t = 18$, the pulse spans approximately 35 grid points in a grid of $N = 400$ points, thus it is always well resolved, in spite of the fact that the grid points spread farther apart towards the outer edge.

For the same initial data, Fig. 4 shows the behavior of U^+ in time, from the initial profile (lower right edge of the figure) as the pulse moves towards the outer boundary (time runs up along the lower left edge of the figure). At $t = 25$, the pulse has crossed the outer boundary and left the grid. The behavior is consistent with an outgoing field in the presence of very weak lower-order coupling to a zero-speed field (see Eq. (32d)). Clearly visible in Fig. 4 is the change in propagation speed, as per Eq. (32d), which increases as the field propagates out towards decreasing β^r values. This behavior is also visible in Fig. 3, with the outgoing component of ϕ consisting mainly of the contribution from U^+.

Figure 5 shows the behavior of U^- in time, from the initial profile at $t = 0$ along the lower right edge of the figure, as the pulse moves towards the left boundary, until $t = 25$. By $t = 5$, the pulse has crossed the inner boundary and left the grid. This behavior is consistent with an incoming field in the presence of very weak lower-order coupling to a zero-speed field (see Eq. (32e)). It is clear from the graph that the incoming field U^- travels at constant velocity -1.

In all cases, there is no observable reflection of either of the fields ϕ, U^+ or U^- from the inner or the outer boundary.

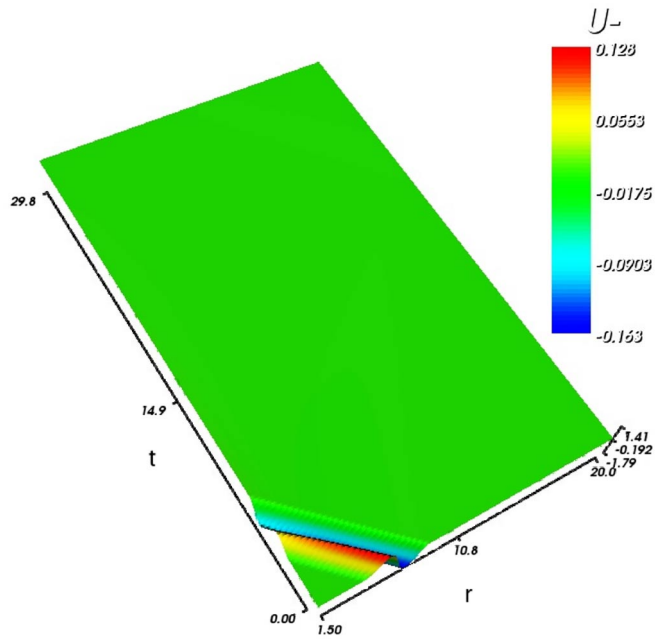

FIG. 5 (color online). Evolution of U^-, scaled by a factor of 10, from $t = 0$ until $t = 25$. Note that by $t = 5$ the ingoing pulse has crossed the inner boundary of the grid.

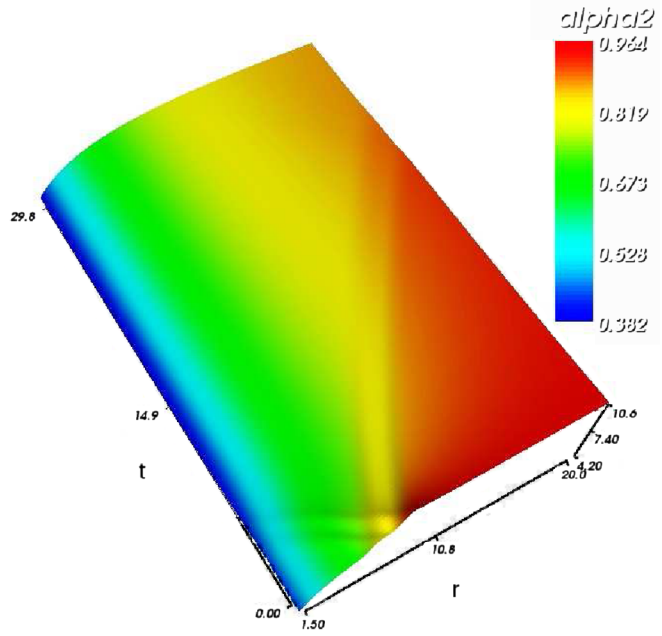

FIG. 6 (color online). Evolution of α^2, scaled by a factor of 10, from $t = 0$ until $t = 25$, by which time the initial pulse in ϕ has either fallen into the black hole or it has crossed the outer grid boundary.

Figure 6 shows the behavior of α^2 in time, from the initial distorted black-hole configuration at the lower right edge of the figure to a time where the black hole relaxes to the final configuration. The initialization process solves the constraint (33a) for α while keeping β^r at Schwarzschild values, hence all the distortion is in the metric function α. As the scalar field propagates through the grid, some of it falling into the black hole and the rest being radiated away, the distortion transfers back and forth from α to β^r, until the metric settles down into the configuration corresponding to a black hole with larger mass. In this figure the effects of the coupling of the lapse to the outgoing field U^+ through driving (undifferentiated) terms are very prominent. The lapse is formally classified as an incoming field, yet it does develop a significant outgoing component which can be seen traveling out and leaving the grid at about $t = 20$.

The behavior of β^r as a function of time from the initial slice until the final time $t_f = 25$ is shown in Fig. 7. By far, the most interesting information to be gathered from the shift's behavior is the location of the horizon. This is explained in the next subsection.

G. Tracking the horizon in a nonlinear dynamical situation

In the Bondi-Sachs gauge, the horizon is located where the shift β^r takes the value $\frac{1}{2}$. Initially, the horizon is located at $r = 2$. As part of the energy of the scalar field

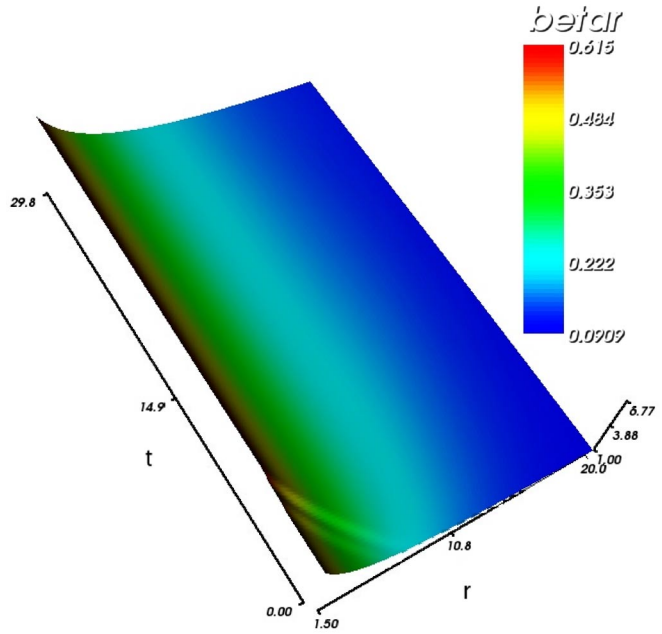

FIG. 7 (color online). Evolution of β^r, scaled by a factor of 10, from $t = 0$ until $t = 25$, by which time the initial pulse in ϕ has either fallen into the black hole or it has crossed the outer grid boundary.

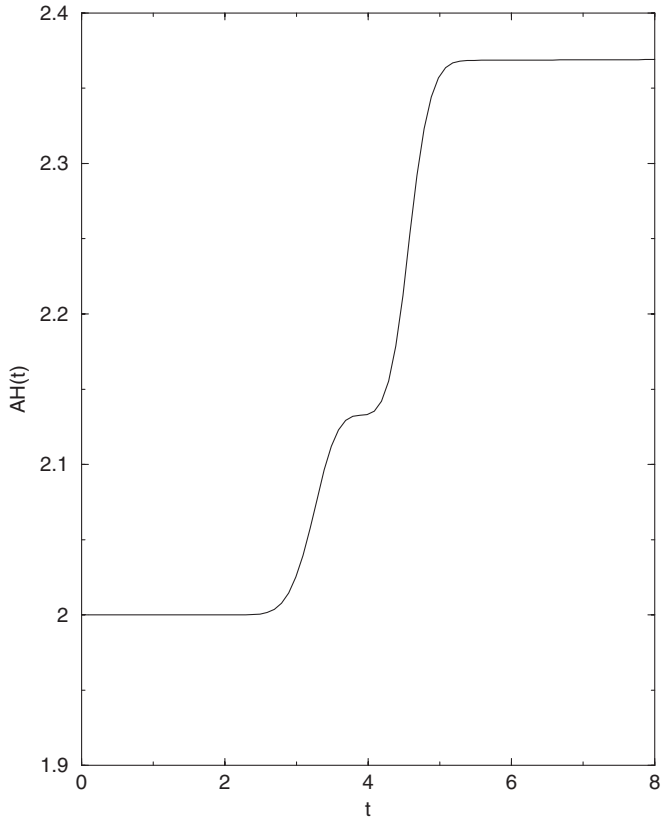

FIG. 8. The apparent horizon r_H, as determined by solving $\beta^r(r_H) = \frac{1}{2}$ during the evolution. Note the jumps in the horizon value as the leading and trailing edge of the pulse fall into the black hole, thus increasing its mass.

falls into the black hole, the horizon increases in area, and this increase can be tracked as a function of time.

This behavior is clearly seen in Fig. 8. We show here only the early part of the evolution. Note the "steps" clearly visible in the profile, corresponding to the leading and trailing edge of the pulse (where the energy is contained) falling into the black hole. After the last time shown here, the profile remains essentially constant, except for small increments in the black-hole mass that register when reflections off the outer boundary (due to numerical noise) reach the apparent horizon. (Such reflections converge away with increasing resolution.)

Figure 9 illustrates the change in area, for the same initial data discussed in previous subsections. The graph shows the shift β^r at $t = 0$ (solid line) and at $t = 25$ (dotted line). At the later time, the horizon is at $r_H = 2.3706$. Identifying the later configuration with a Schwarzshild black hole leads us to a mass $M = r_H/2 = 1.1853$. The shift of an $M = 1.1853$ Schwarzshild black hole is in excellent agreement with the profile at the later time.

Figure 10 shows a similar plot for the lapse function α, displaying the change in the square of the lapse, α^2,

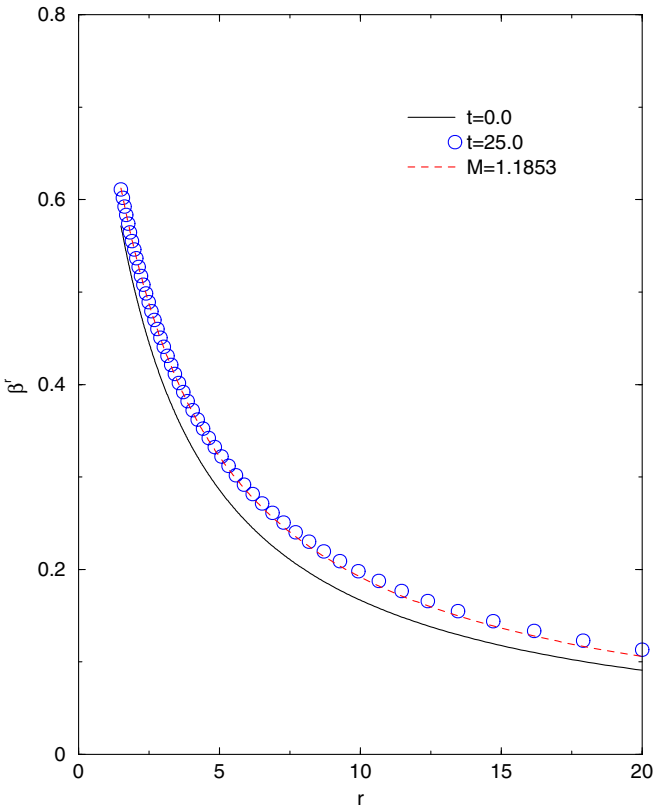

FIG. 9 (color online). The shift β^r, showing the change in the location of the horizon, $\beta^r = \frac{1}{2}$, from $r = 2$ initially ($t = 0$, solid line), to $r = 2.3706 \equiv 2M_f$ at $t = 25.0$ (circular markers). The final profile is overlaid with the shift for a Schwarzschild black hole of mass $M = 1.1853$ (dashed line), showing excellent agreement.

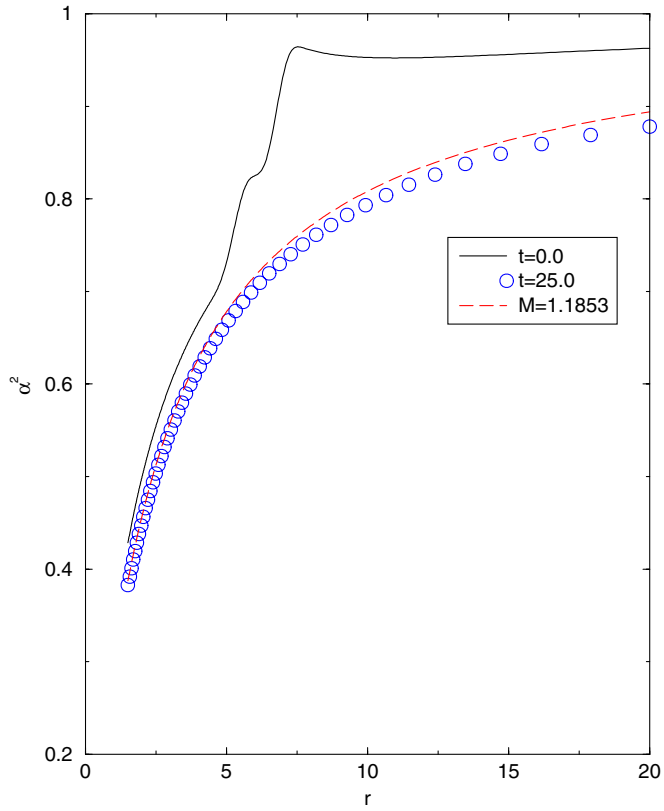

FIG. 10 (color online). Change in the lapse α for a pulse of the form (36) with amplitude $A = 5 \times 10^{-2}$, and support between $r_1 = 4$ and $r_2 = 8$. The initial (solid line) and final profile (circular markers) are shown. The final profile is in good agreement with the lapse for a Schwarzschild black hole of mass $M_f = 1.1853$ (dashed line), corresponding to black-hole mass read from the condition $\beta^r = \frac{1}{2}$ at $t = 25$.

between the initial and final configuration for the same initial data. The initial configuration, the solution of the initial constraint, deviates significantly from the profile expected from a Schwarzschild black hole, which is clear evidence of the nonlinearity of the situation considered. At the last time shown, where most of the energy of the field has either fallen into the black hole or has been radiated out of the grid, the lapse approaches the profile corresponding to a black hole of mass $M_f = 1.1853$, in agreement with the value of M_f obtained from the shift β^r. Note however that, because there is still a small amount of scalar field left outside the horizon, we do not expect to see *perfect* agreement between the evolved profiles for α and β^r and the corresponding metric functions for a Schwarzschild black hole of mass $M_f = 1.1853$.

H. Conservation of the constraints

The constraint (33a) is not enforced during the numerical simulation, but is preserved by the evolution scheme. It should then converge to zero to the order of the discretization used. To verify convergence of the constraint to second

order (which is the order of the spatial discretization), we plot in Fig. 11 the constraint (33a) for the same four grid sizes used in Fig. 2 at time 3.0, i.e., at a time where the fields U^+ and U^- have not yet left the grid, and most of the constraint violation is located near the black-hole horizon. We plot, as a function of the radial coordinate r, the difference of the constraints between consecutive finer grids, e.g. $C_{200} - C_{400}$, scaled by the square of the grid refinement ratio with respect to the coarsest grid (200 points). The profiles for the three different curves (shown as dashed, dotted and solid lines in the graph) are scaled by factors of 1, 4 and 16, respectively. The scaled profiles overlap as expected, confirming that the constraint is indeed preserved and converges to second order.

Figure 12 shows the constraint C, monitored during the evolution of the same pulse. It is clear from the graph that the constraints propagates inward, with speed -1, as indicated in (17). The constraint on the initial time (not shown) is zero, since Eq. (33a) has been used to solve for the initial lapse α^2. Its profile at subsequent times is consistent with the location of the pulse, and propagates inwards towards the left grid boundary, without any visible reflections. At later times, i.e. $t \approx 25$, there is a visible contribution arising on the outermost grid boundary, which

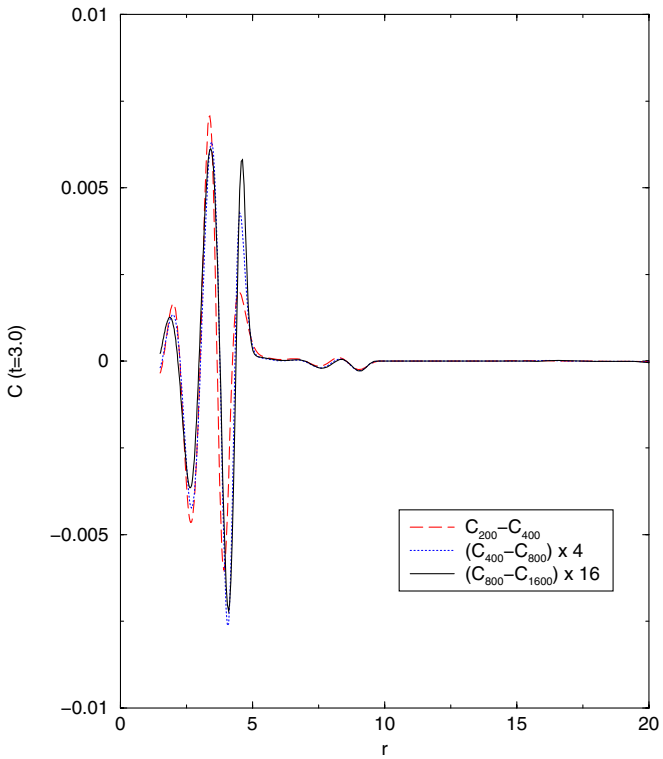

FIG. 11 (color online). Convergence of the constraint (33a), illustrated at $t = 3.0$. The four grid sizes used in Fig. 2, 200, 400, 800 and 1600 points, are used. We plot the difference between consecutive grids, scaled by the appropriate factor. The differences overlap, confirming second-order convergence of the constraint.

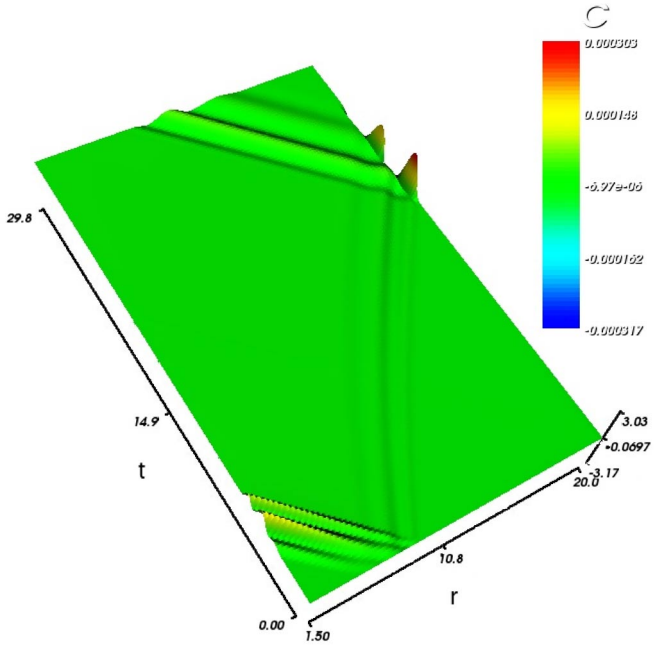

FIG. 12 (color online). The constraint, Eq. (33a), scaled by a factor of 10^4, monitored during the evolution, shows the proper propagation speed of -1, as per Eq. (17). There is an *outgoing*, component essentially determined by the field U^+. The *incoming* feature seen at later times arises from the interaction of this component and the outer boundary condition.

eventually propagates inwards. Readers with a lay background in numerical techniques should not regard these ''constraint violations'' as actual violations of the constraint in the evolution of the continuous equations, since, by our convergence analysis of the previous paragraph, these apparent constraint violations converge to zero in the order of the discretization. Still, they are useful in illustrating the propagation of real constraint violations (larger than the order of the discretization), should one choose to implement them.

Strictly speaking, Fig. 11 shows that the constraint converges to some value, but not necessarily to zero. We argue that convergence to a value other than zero can not happen if the discretization of the system of equations is consistent. To show that the constraint does in fact converge to zero, we need simply look at the constraint values as a function of grid size, and to verify that the constraint effectively decreases with increasing resolution. We would expect the constraint to converge to the same order as the discretization of the evolution equations, provided that not just the fields, but also the derivatives (which enter in the constraint) are also in the convergence regime.

In addition, Fig. 11 shows the constraint (rather, their relative differences) at a time when the pulse has not yet left the grid, and it does not address the question of whether the boundary condition has any effect on convergence of the constraint at later times. This can be decided by looking

at the maximum absolute value of the constraint over the grid as a function of time for various grid sizes ($N = 1000$, 2000 and 4000 points), as displayed in Fig. 13. The graph shows that the constraint is in fact bounded during the evolution and that it decreases with increasing resolution, as expected, even during and after the pulse goes through the outer boundary.

In Fig. 14 we show the constraint at various grid sizes ($N = 400$, 800 and 1600 points), at $t = 30$, a time at which any effect introduced by the boundary condition would be manifest. The constraint over the grid clearly decreases with increasing resolution, even after the outgoing part of the scalar pulse has crossed the boundary and the boundary condition has clearly been used. The boundary condition can be said, in this respect, to be *constraint preserving*.

We show also in Fig. 15 the profiles of the constraint at $t = 30$ for three different resolutions: $N_c = 2000$ (circles), $N_m = 2500$ (squares) and $N_f = 3000$ (continuous line). The lines in the plot have been appropriately scaled, i.e. multiplied by a factor of $((N_i - 1)/(N_f - 1))^2$, recall that the grid spacing is inversely proportional to $N - 1$, and thus we would expect the profiles for the three resolutions to agree after this rescaling, if the constraint converges to zero to second order, as in fact we see in Fig. 15.

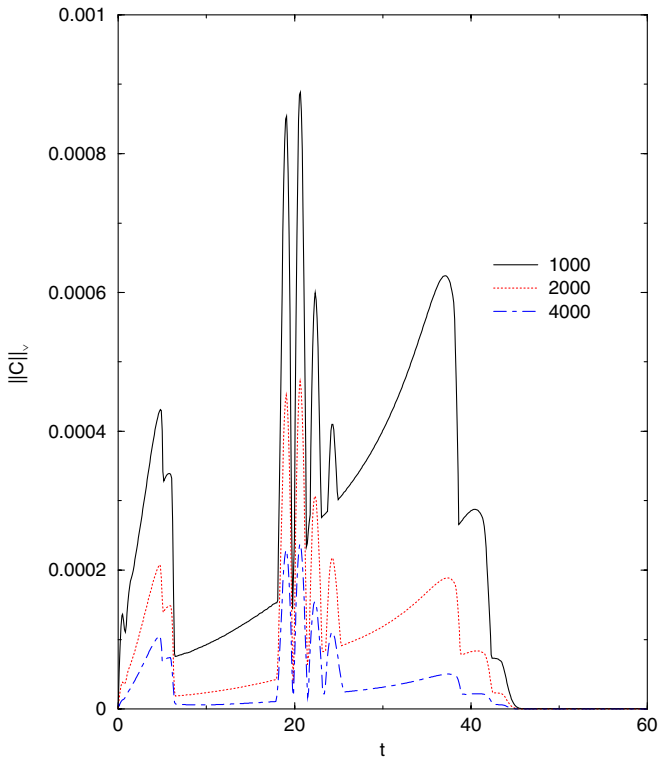

FIG. 13 (color online). The maximum absolute value of the constraint over the grid, $|C|_\infty$ as a function of time, for the resolutions $N = 1000$, 2000 and 4000. The graph shows that the constraint violation decreases with increasing resolution during the entire evolution, even after the outgoing part of the pulse has crossed the outer boundary.

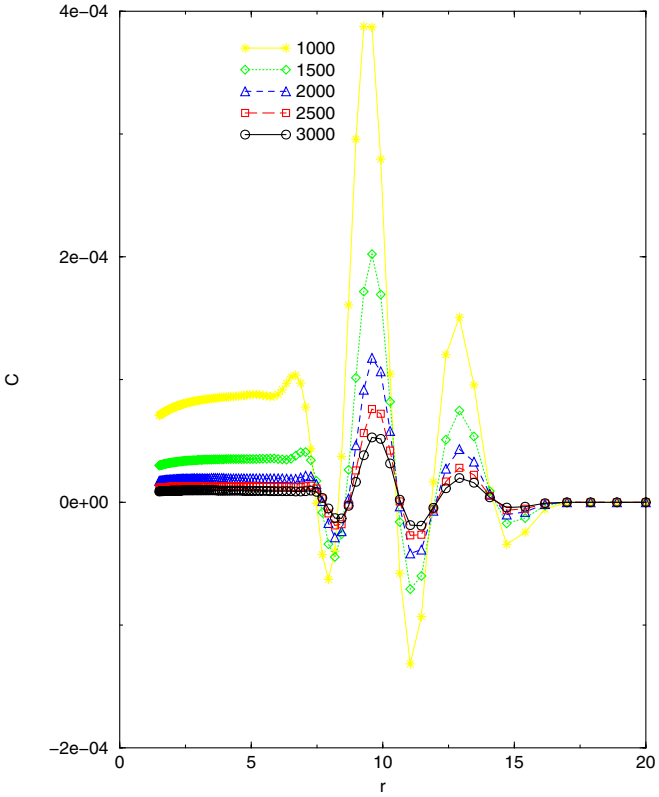

FIG. 14 (color online). The constraint, Eq. (33a), shown here at $t = 30$ on various grids sizes. The graph shows that the constraint violation decreases with increasing resolution, at a time when the outgoing part of the pulse has crossed the outer boundary.

Further insight on the nature of the solution at later times can be gleaned from Fig. 16, which shows the scalar field at $t = 30$ at three resolutions: $N_c = 400$, $N_m = 800$ and $N_f = 1600$. The lowest resolution shows clearly visible oscillations in the range $4 < r < 9$. However, the amplitude of these oscillations decrease rapidly with increasing resolution, so they can be seen to be discretization errors which converge to zero. Furthermore, when we track these oscillations back in time, we see that they originate at the front and tail end of the initial pulse.

It is clear that errors in the computation of the fields lead in turn to constraint violations, but provided these errors are also convergent, this is not a problem, and should in fact be expected. The error for a given resolution, to a good approximation, can be estimated as the difference between the profile at that grid size and that of a reference run with $N = 3000$ points. Figure 17 shows the estimated errors on the scalar field for the same grid sizes of Fig. 16, appropriately scaled to demonstrate proper second-order convergence. Similar behavior can be seen for the remaining fields (α^2, β^r, U^+, U^-), not shown here. The relation between the second-order convergent error of the scalar field (and of the remaining fields) and that of the second-order convergent constraint is naturally obscured by the

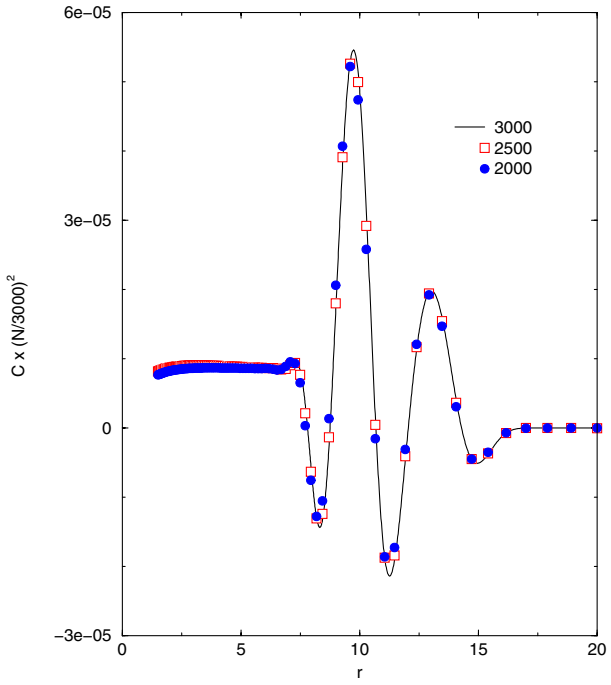

FIG. 15 (color online). The constraint, Eq. (33a), at $t = 30$ on three grid sizes, $N_c = 2000$ (circles), $N_m = 2500$ (squares) and $N_f = 3000$ (continuous line), scaled by a factor of $((N_i - 1)/(N_f - 1))^2$, for $N_i = N_c, N_m$. The three profiles (appropriately scaled) overlap, confirming that the constraint converges to second order on the discretization over the entire grid.

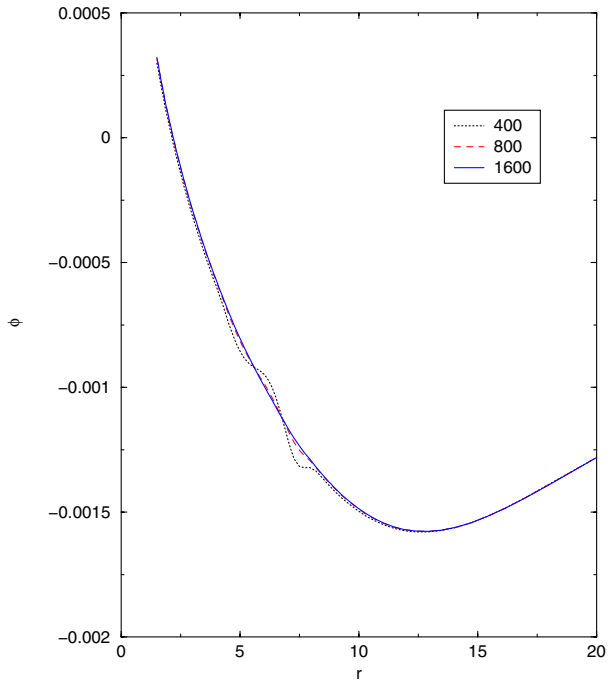

FIG. 16 (color online). The scalar field ϕ at $t = 30$ at three resolutions: $N_c = 400$, $N_m = 800$ and $N_f = 1600$. The oscillations seen in the lower resolution run clearly decrease with increasing resolution.

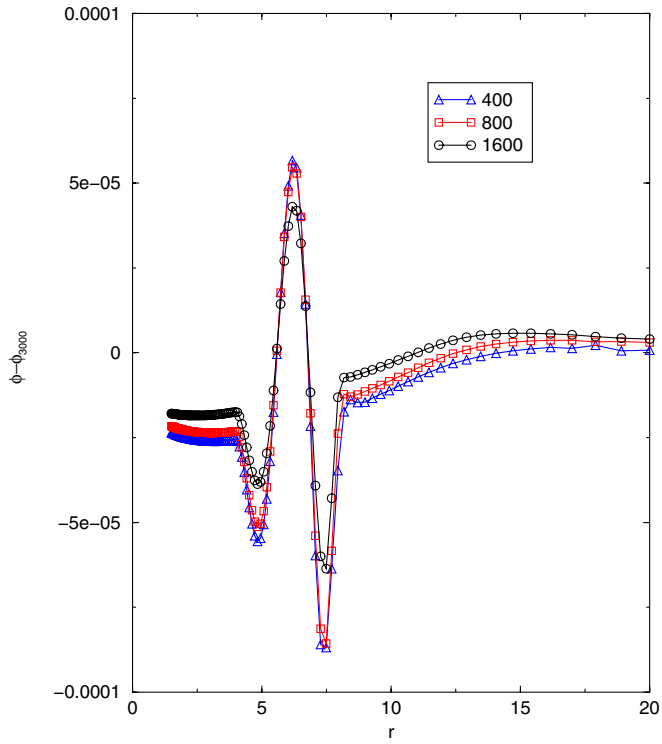

FIG. 17 (color online). Error in the scalar field ϕ at $t = 30$ at the three resolutions of Fig. 16, measured as the difference between the profile at that resolution and that of a reference run with $N = 3000$ points. The errors have been rescaled (multiplied) by 1 (N_c), 4 (N_m) and 16 (N_f).

differential nature of the constraint. Nevertheless, we hope the present discussion makes it clear that they are indeed related, that is, for a well-posed initial-boundary value problem with boundary conditions which preserve the constraints, any constraint violation which results from discretization errors will converge to zero as the simulation becomes better resolved. We stress that we do not claim to have presented a boundary condition that is a perfect absorber (so that no field is reflected at the boundary). Any constraint violation present at the discretization level may "bounce" off the boundary. In fact, there is a clearly visible incoming constraint violation in Fig. 12, which appears to originate at the boundary. This, we believe, is a product of the interaction of the discretization error in the outgoing scalar field component (see Fig. 3) with the boundary. We have shown however that the constraint violation converges to zero with increasing resolution.

VIII. REMARKS AND OUTLOOK

The assumption of spherical symmetry has always been valuable as a tool to understand diverse aspects of the Einstein equations. And in spite of its frequent recurrence, it still has not exhausted its power to illuminate new applications, as it keeps up with the general progress in the field. Our current presentation of the properties of the

Bondi-Sachs gauge, for instance, allows us to extract a rich structure which passed unnoticed in rare earlier presentations, such as that of [9].

At the most fundamental level, we have essentially demonstrated how to bridge a conventional divide between two formalisms in current use for numerical simulations of black-hole spacetimes: the Bondi-Sachs (or characteristic) approach and the ADM (or 3 + 1) approach. On the one hand, for practitioners of the Bondi-Sachs approach this entails a deeper understanding of the mechanisms of characteristic evolution and may potentially provide insights into the nature of the required data. On the other hand, clearly, it is the ADM approach that benefits the most from this exercise by acquiring a well-posed hyperbolic form. Emphasis should be placed on the fact that nothing at all has been done to modify the standard ADM equations or variables in order to accomplish this; we have merely imposed a certain gauge choice on the standard scheme (the Bondi-Sachs gauge). It is worthwhile pointing out that, as the Bondi-Sachs gauge has a dynamical shift—that is, prescribed by evolution equations coupled to the other fields—this work goes beyond basic studies of constraint-preserving boundary conditions, where the shift is prescribed arbitrarily (and, most commonly, vanishing) [10,11,16–19].

We have also demonstrated that the resulting form of the ADM problem is very well suited for numerical simulations of dynamical black-hole spacetimes. A novel feature of our work—not present in other well-posed renditions of spherically symmetric 3 + 1 problems for the Einstein equations such as [11] or [16]—is the successful numerical implementation of an exact constraint-preserving boundary condition in the case of a dynamical black-hole spacetime, that is, where both the metric and the matter fields are allowed to interact and evolve.

Admittedly the simplifications brought about by the assumption of spherical symmetry may have a large role to play in both the analytic and numerical properties of the resulting system of evolution equations. But the ultimate goal of this project is to remove the restriction of spherical symmetry and examine the ADM problem in the Bondi-Sachs gauge in full generality. We think that there are reasonable indications that the three-dimensional problem will inherit some of the most characteristic properties of the spherically symmetric rendition, such as a significantly reduced number of fundamental variables and the ability to identify at least a subset of characteristic fields. As for nontransferable traits, most likely, the three-dimensional ADM equations in the Bondi-Sachs gauge will not be automatically of first order even in the time and radial space, so a reduction to first-order will need to be implemented for all variables other than the lapse and the radial component of the shift. The reason for this is that none of the Bondi-Sachs equations other than those for V and β are of first-order in the radial and time coordinates (see, for instance, [20]).

As a stand-alone problem, nevertheless, the ADM formalism coupled to a scalar field in spherical symmetry turns out to be a valuable resource for the study of black-hole physics and of the mathematics of partial differential equations. As we demonstrate with our numerical simulations, interesting behavior related to the dynamics of apparent horizons can easily be illustrated, as well as the behavior of characteristic fields of nonlinear symmetric-hyperbolic inhomogeneous systems of partial differential equations, all without the need for any special handling of the numerical code beyond the most standard techniques. For this reason, we think that even in its restrictive simplicity, this problem is naturally endowed with significant intrinsic value.

ACKNOWLEDGMENTS

This article grew out of a question by David Garfinkle at the 22nd Pacific Coast Gravity Meeting, held at KITP, UCSB, Santa Barbara, California, March 3-4 2006. This research was supported by the National Science Foundation under grant No. PHY-0244752 to Duquesne University. Computer time was provided by the Pittsburgh Supercomputing Center under grant No. PHY-060004P. We thank Greg Foss for his assistance with visualization.

[1] S. Frittelli, Phys. Rev. D **73**, 124001 (2006).
[2] R. K. Sachs, Proc. R. Soc. A **270**, 103 (1962).
[3] R. Gómez *et al.*, Phys. Rev. Lett. **80**, 3915 (1998).
[4] R. Gómez, L. Lehner, R. Marsa, and J. Winicour, Phys. Rev. D **57**, 4778 (1998).
[5] I. Racz, Class. Quant. Grav. **23**, 115 (2006).
[6] J. W. York, in *Sources of Gravitational Radiation*, edited by L. Smarr (Cambridge University Press, Cambridge, England, 1979).
[7] B. Gustaffson, H.-O. Kreiss, and J. Oliger, *Time-Dependent Problems and Difference Methods* (Wiley, New York, 1995).
[8] M. W. Choptuik, Phys. Rev. Lett. **70**, 9 (1993).
[9] R. Gómez, R. Marsa, and J. Winicour, Phys. Rev. D **56**, 6310 (1997).
[10] S. Frittelli and R. Gómez, Phys. Rev. D **69**, 124020 (2004).
[11] S. Frittelli and R. Gómez, Class. Quant. Grav. **20**, 2379 (2003).
[12] J. Thornburg, gr-qc/0512169.

[13] L. E. Kidder, M. A. Scheel, and S. A. Teukolsky, Phys. Rev. D **64**, 064017 (2001).
[14] R. Gómez, R. Isaacson, and J. Winicour, J. Comp. Phys. **98**, 11 (1992).
[15] W. H. Press, S. A. Teukolski, W. T. Vetterling, and B. P. Flannery, *Numerical Recipes in Fortran* (Cambride University Press, Cambridge, England, 1992), 2nd ed..
[16] G. Calabrese, L. Lehner, and M. Tiglio, Phys. Rev. D **65**, 104031 (2002).
[17] S. Frittelli and R. Gómez, Phys. Rev. D **68**, 044014 (2003).
[18] G. Calabrese, J. Pullin, O. Reula, O. Sarbach, and M. Tiglio, Commun. Math. Phys. **240**, 377 (2003).
[19] S. Frittelli and R. Gómez, Phys. Rev. D **70**, 064008 (2004).
[20] R. Gómez and S. Frittelli, Phys. Rev. D **68**, 084013 (2003).